Radiation-Induced Changes in Single Crystal Calcite and Dolomite, Mineral Analogues of Light Water Reactor, Nuclear Power Plant Concrete Aggregates

Chinthaka M. Silva, [1, 2, *] Thomas M. Rosseel, [2] Kiel S. Holliday [1]
[1]*Lawrence Livermore National Laboratory, Livermore, CA 94550, USA*
[2]*Materials Science and Technology Division, Oak Ridge National Laboratory, Oak Ridge, TN 37831, USA*

1.0 Abstract

Two analogues of aggregates (calcite and dolomite) found in nuclear power plant (NPP) concrete have been neutron irradiated to fluences up to 2×10^{20} n/cm^2 at 52 °C and 4×10^{19} n/cm^2 at 95 °C (E>0.1 MeV). X-ray diffraction studies showed that these aging conditions affected crystallography of both calcite and dolomite, with both showing a growth in their unit cells compared to that of the unirradiated samples. Only dolomite samples showed a continuous increase of its lattice parameters with the increase in irradiation. In calcites, the lattice growth with irradiation dissipated after a fluence of 5×10^{18} n/cm^2. Radiation-induced disordering of the crystal structure was observed in both materials, while a healing effect of irradiation temperature was mainly observed in calcites. Dislocation densities calculated using XRD data also supported these observations. Insights made into the unit cells of both minerals using Fourier synthesis showed that the Mg sites are more prone to the neutron irradiation than the Ca sites resulting in larger radiation effects and higher disruption in the crystal structure of dolomite than that of calcite. Other than the polycrystalline characteristics observed using TEM, these minerals did not show complete amorphization or significant structural decomposition at the studied irradiation fluences.

**This manuscript has been co-authored by the Lawrence Livermore National Laboratory (LLNL) under contract DE-AC52-07NA27344 and UT-Battelle, LLC, (ORNL) under contract DE-AC05-00OR22725 with the US Department of Energy (DOE). The US government retains and the publisher, by accepting the article for publication, acknowledges that the US government retains a nonexclusive, paid-up, irrevocable, worldwide license to publish or reproduce the published form of this manuscript, or allow others to do so, for US government purposes. DOE will provide public access to these results of federally sponsored research in accordance with the DOE Public Access Plan (http://energy. gov/downloads/doe-public-access-plan).

*Corresponding author: Chinthaka M. Silva, silva228@llnl.gov

Key words: calcite; dolomite; neutron irradiation; nuclear power plant

2.0 Introduction

In order to fulfill the demand for clean (non-carbon) electric power, the extended operation of the existing US light water reactor (LWR) nuclear power plants (NPPs) beyond 60 and possibly 80 years is under evaluation. [1, 2] Extending the life cycle of the currently operating US NPP fleet requires research-based evaluations of the corresponding structures to fill knowledge gaps based on the development of databases of irradiation behavior of materials of interest. Among the materials-related aging issues being addressed, the behavior of concrete structures is of high importance because concrete is used in NPPs for radiation shielding and reactor pressure vessel supports. Although investigations on radiation behavior of concrete have been reported, especially on mechanical properties, the effects of neutron doses compatible with extended use at reactor operating temperatures were sparsely studied. This limits the knowledge of the behavior of NPP structures under long-term irradiation aging conditions and has been of great interest to the research community.[3, 4, 5, 6] The concrete structures of the currently operating US NPPs are composed of Portland cement, which is made using high-calcium limestone, clay, sand, and a small amount of iron ore in a cement kiln,[7] and ~ 70% by volume of site-specific aggregates composed of various minerals including silicates, carbonates, and oxides. Therefore, the research conducted on concrete and as well as its aggregates is important.

Maruyama et al. reported hypothesized radiation-induced degradation of concrete as a result of metamictization, which is usually referred to the amorphization of minerals due to radiation effects, and swelling of its mineral aggregates (e.g., quartz, feldspars, and limestone).[8] However, no evidence of significant physical property changes such as sample expansion was reported in limestone neutron irradiated to ~10^{19} n/cm^2 (E>0.1 MeV) fluences. They also reported interactions of gamma radiation, which results from neutron irradiation, with hydrates and water molecules bound in the cement as an important factor of stability of cement paste. Therefore, studying the irradiation behavior of separate concrete aggregates is also relevant. In some cases, irradiation behavior of reinforced concrete (RC), which is used as biological shielding and reactor pressure vessel supports, has also gained attention and shown that prolonged aging under neutron irradiation can degrade it, and therefore could be critical, based on mechanical properties.[9] In addition to neutron irradiation studies of calcites and dolomites, the literature also discusses their behavior under various radiation conditions. For example, Kabacinska et al. showed surface-based amorphization in calcite that was irradiated using UV radiation, while X-ray and γ radiation effects were less prominent.[10]

Specifically, analogues of the reactor cavity concrete have been studied under irradiation conditions at and above the expected neutron doses [11] at extended operation of the US LWR fleet. Moreover, this research has expanded and developed into internationally recognized collaborative efforts [8, 12, 13, 14]. Under these efforts, neutron irradiation of some selected neutron doses at varied temperatures and

studying its effects on concrete aggregates have been carried out by the US national laboratories and universities. [3, 12, 18] The three commonly found minerals in concrete aggregates, alpha quartz (SiO_2), dolomite ($CaMg(CO_3)_2$), and calcite ($CaCO_3$) were selected for the irradiation study using Seeberger and Hilsdorf [15] as a guide. The choice of quartz and carbonates was based on the observation by Field et al. [16] that silicates, such as quartz, exhibit large expansion while carbonates have limited expansion. Also, due to high concentrations of calcite and dolomite (>95% in some geographic locations),[17] the characterization of calcite and dolomite behavior under long-term aging thermal and irradiation conditions in NPPs requires a detailed investigation. Therefore, the study of radiation-induced crystallographic and microstructural effects on single crystal calcite and dolomite are presented here, while the study performed on α-quartz was reported earlier.[18]

3.0 Experimental details

3.1 Sample preparation and their irradiation

The two single crystal calcite and dolomite carbonate mineral boules were cut into 24 samples using a Buehler IsoMet slow-speed saw with nominal dimensions of 9.5×4×1.3 mm. An MTI diamond wire saw was used to prepare additional samples for unirradiated baseline measurements. The maximum dimensions of specimens were determined by the capsule geometries and the estimated maximum swelling (<5%) at the highest neutron dose and the loading of sets of four specimens of each material at the same horizontal position within a capsule.[16] Each sample was engraved or marked with a unique identification to ensure proper tracking.

Calcite and dolomite samples were irradiated to three different basic neutron doses (5×10^{18}, 4×10^{19}, and 2×10^{20} n/cm^2 at E>0.1 MeV) and two different temperatures (52 and 95 °C in perforated and sealed capsules, respectively) at the Oak Ridge National Laboratory (ORNL) High Flux Isotope Reactor (HFIR). These conditions were used to reflect irradiation levels equal to those expected at proposed extended operation on the biological shield of NPPs. A summary of the irradiation fluences of the samples presented here is shown in Table 1. The rounded irradiation fluence values will be used in the rest of text henceforth.

Table 1. Calcite and dolomite samples irradiated at HFIR.

#	Sample	Irradiation fluence (n/cm^2, E>0.1 MeV)	Irradiation temperature (°C)
		Calcites	
1	C4	4.92×10^{18}	52
2	Cb	3.94×10^{19}	52
3	C6	1.97×10^{20}	52
4	C18	5.04×10^{18}	95
5	C10	4.03×10^{19}	95
		Dolomites	
1	D15	3.94×10^{19}	52
2	Dd	1.97×10^{20}	52
3	D18	5.04×10^{18}	95
4	D13	4.03×10^{19}	95

3.2 Powder X-ray diffraction (XRD)

Powder XRD samples were prepared by grinding a small piece of the pre- and post-irradiated single crystals of calcite and dolomite using a mortar and pestle. All the samples were prepared using this same procedure to avoid any relative errors associated with the technique. This powder technique was also used to minimize any texture associated with the precursor single crystals and to obtain a flat-thin layer of the sample admixed with a standard in acquiring a proper correction to any displacement error. Furthermore, the powdered samples were mounted on a low background quartz or a zero-background Si diffraction plate bought from MTI Corporation, California, USA. Adding several drops of isopropyl alcohol, a thin layer slurry of the powder was prepared on the plate. After drying off the alcohol, the sample mount was sealed using a Kapton tape to prevent dispersion of any radioactive material out of the plate. The sample was then scanned over a ~19 h time period with a step size of 0.005 over 10 – 120° 2Theta range using either a Scintag or a Bruker D2 Phaser Benchtop powder X-ray diffractometer to obtain a powder XRD pattern. The Scintag diffractometer was operated at 40 kV and 40 mA and the D2 Phaser at 30 kV and 10 mA with Cu Kα radiation. An internal standard (LaB_6 SRM 660b or Si SRM640b) was incorporated in the samples when acquiring XRD patterns for lattice parameter refinements using GSAS [19] software.

Example XRD patterns of the unirradiated (control) samples of calcite and dolomite together with their Rietveld analyzed fits are shown in supporting information (Figure S1). The impurity peak identified at 26.65° 2θ together with slight humps at 26.5 and 27.4° 2θ values (Figure S1a) indicate that the calcite sample has some impurity secondary phases that are mostly Aragonite (ICSD #15194)), an orthorhombic polymorph of trigonal calcite, with minor amounts of Vaterite (ICSD #15879), a hexagonal polymorph. A second calcite sample collected from another control sample showed an impurity peak ~28.1 °2θ and the absence of impurity peaks previously mentioned, indicating inconsistency in the impurity phases of the precursor samples. These impurity peaks were not identified in the irradiated calcite samples. Therefore,

any effects of impurity chemical phases on the results discussed herein was assumed to be negligible. No apparent impurity peaks were observed in the dolomite samples (Figure S1b).

Jana2006 was used for profile fitting followed by Fourier synthesis.[20] Electron density maps calculated using observed (F_O)-Fourier synthesis were drawn using ChimeraX.[21] These electron density maps were drawn in 3D space as volumes enclosed by isosurfaces, and the corresponding estimation of volumes was also carried out within ChimeraX. Difference Fourier synthesis was also used on summed electron density observation using contour type maps. Crystallite size and microstrain (or lattice strain) of the samples were determined using the Scherer equation and Williamson-Hall (W-H) method, respectively. These two methods are described in-detail elsewhere.[22] Dislocation density of the samples was estimated using dislocation density functions of microstrain and coherent domain size (or crystallite size) described by Holt et al.[23] Microstrain for these calculations was determined using the Bragg reflections up to ~70° 2Theta. Bragg reflection corresponding to (104) Miller index at ~30° 2Theta was used in both calcite and dolomite samples as it has high peak intensity and has no apparent faults. The reflections (116) at ~48.5° and (113) at ~41° 2Theta values were also used to estimate dislocation densities of calcite and dolomite samples, respectively, to cover both low- and high-angle reflections. Two-dimensional visualization of calcite and dolomite unit cell structures was performed using VESTA visualization software.[24]

3.3 Transmission electron microscopy (TEM)

Both calcite and dolomite samples used in TEM investigations were prepared using a solution-drop method. In this method, a powdered sample was first immersed in an alcohol solution, which was mixed or sonicated to obtain a homogeneous distribution of particles. Some fine particles of the sample were then transferred to a 3 mm TEM grid using a small-tipped pipette as described in an earlier paper.[25] These TEM specimens were characterized using a 2100F JEOL TEM operated at 200 kV field emission gun. Imaging was performed using bright field (BF) and dark field (DF) and at both low resolution (LR) and high resolution (HR) TEM modes. Selected area electron diffraction (SAED) was also used to investigate sample characteristics with respect to crystallinity.

4.0 Results

4.1 X-ray powder diffraction

4.1.1 Calcite

A representative selection of the XRD patterns of the samples studied here are shown in Figure 1. Significantly intense peaks corresponding to all the reflections for $CaCO_3$ ($R\bar{3}c$) are observed for the control sample (Figure 1a). As depicted by rest of the XRD patterns in Figure 1, the intensities of the

Bragg peaks of calcite have significantly decreased in the samples that were neutron irradiated at both 52 and 95 °C with the lowest intensities in the 4×10^{19}, 52 °C sample, indicating a decrease in the long range order of the crystal structure. This is especially apparent in the case of the (006) peak in which the intensity is insignificant with only a hump for the samples irradiated at 52 °C (Figure 1b-d). By comparison, slightly greater peak intensities are observed in the samples irradiated at 95 °C (Figure 1e-f) with similar neutron doses. This observation is more prominent in the samples irradiated to 4×10^{19} n/cm^2. Profile fitting of these XRD patterns also showed that some anisotropic peak broadening is present at peak tails, particularly in 5×10^{18} - 2×10^{20}/52 °C and 5×10^{18}/95 °C samples. One peak in particular (110) is highlighted by a dotted circle in Figure 1; note that this feature was not prominent in the 4×10^{19}, 95 °C sample (Figure 1f). This feature did not show any correlation to the peak widths or the full width at half maximum (FWHM), so it was unable to be characterized quantitatively.

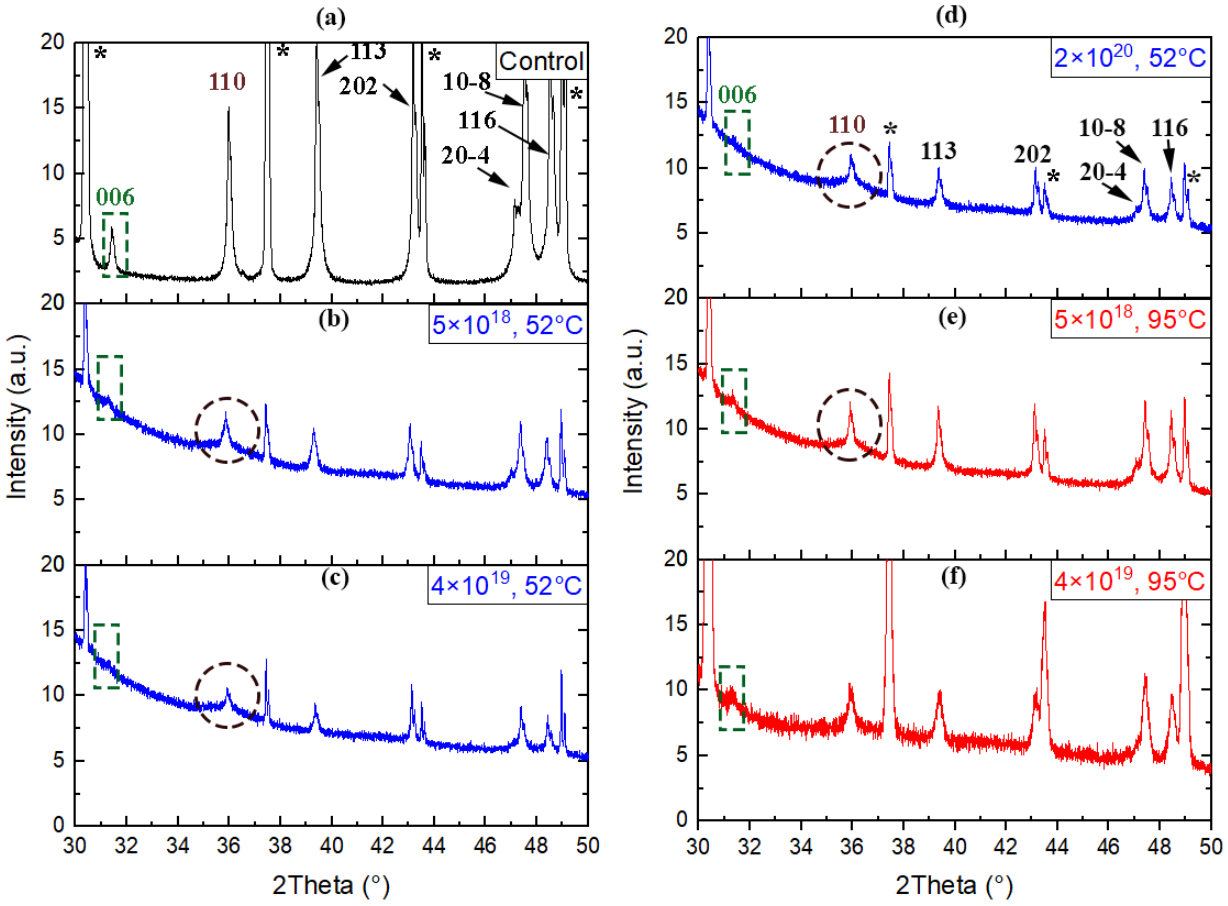

Figure 1. XRD patterns of the calcite samples. Only the 30 – 50° 2θ region is shown as a representation. Millar indices of the $CaCO_3$ reflections are highlighted, and the asterisks indicate some of the reflections of the LaB_6 standard admixed with the samples. Reflections (110 peak) that showed anisotropic peak broadening in the profile fits are highlighted by circles, while rectangular boxes highlight the (006) peak with varied intensities.

Lattice parameters (*a* and *c*) of the neutron irradiated calcite samples both at 52 and 95 °C are greater than that of the unirradiated sample of 4.9834 (1) and 17.0510 (5) Å (Figure 2). The calcite unit cells of the samples irradiated to 5×10^{18} n/cm^2 grow to values greater than ~0.2 % of the unirradiated sample along a-axis (Figure S2a). It then drops to <0.2 % greater value of the unirradiated sample for the samples irradiated to 4×10^{19} – 2×10^{20} n/cm^2 doses. Note that even though these relative values are as low as 0.2%, they are significant enough to indicate actual unit cell size variations as the error associated in the refined lattice parameters are 30 – 600 times lower. Furthermore the increases are slightly greater in the samples irradiated at 52 °C compared to the 95 °C samples at similar neutron doses. Irradiated assisted growth of the calcite unit cell along c-axis is greater compared with that along a-axis; the highest increase in lattice parameter *c* is in ~0.3 – 0.5 % compared with the unirradiated sample. Other than a slight decrease in the 2×10^{20} n/cm^2 dose samples, lattice parameter along c-axis overall increases with the increase in irradiation for both 52 and 95 °C temperatures. Like in the case of lattice parameter *a*, greater lattice parameter *c* values are observed for the samples of closely similar neutron doses and irradiated at 52 °C compared with that of the 95 °C. These lattice expansion results are similar to, although smaller than, the lattice parameter changes observed in neutron irradiated single crystal quartz.[25]

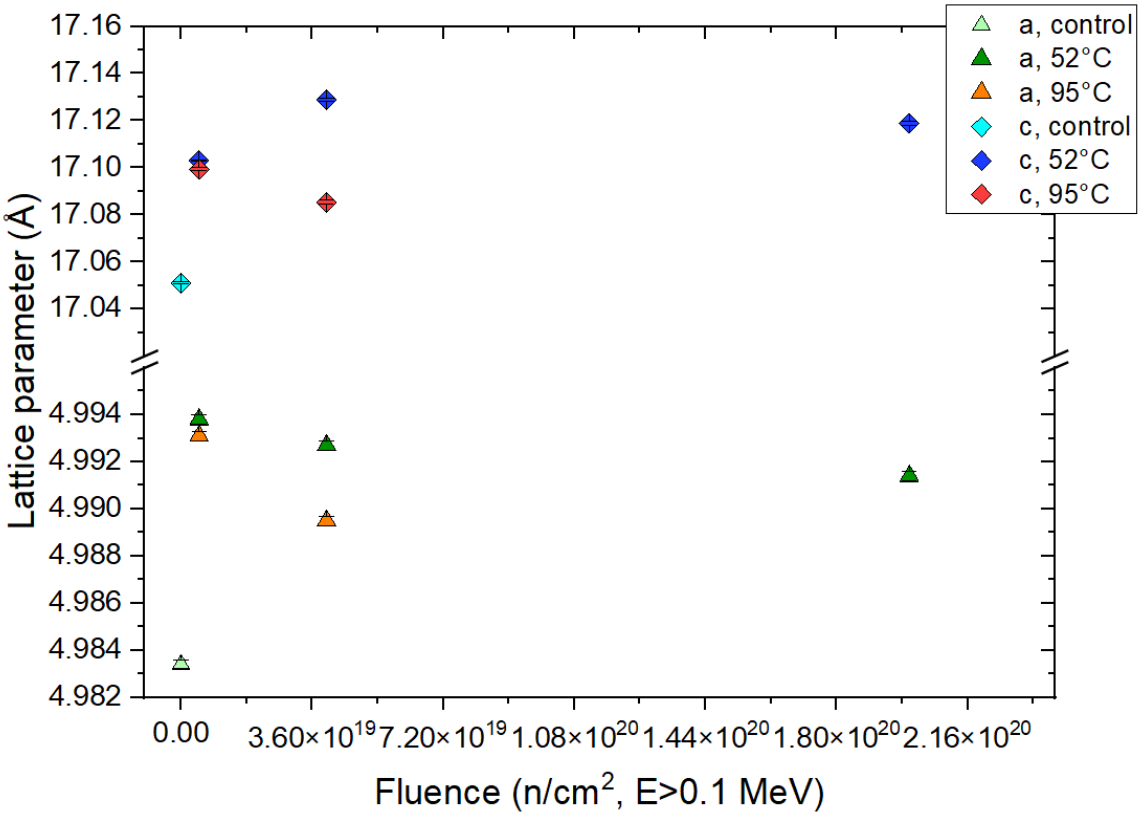

Figure 2. Refined lattice parameters of the calcite samples as a function of irradiation at 52 and 95 °C. Unirradiated sample is also shown.

Because the refined lattice parameters of the irradiated calcite samples are greater than that of the control sample, their unit cell volumes are also greater than the control sample (Table 2). Unit cell volume of the samples irradiated at 52 °C show an increase from 5×10^{18} through 4×10^{19}, while it drops at 2×10^{20} to a value similar to that of the 5×10^{18} n/cm^2 sample within the error in the volume calculations. Among the samples irradiated at 95 °C, a lower unit cell volume is observed in the higher fluence sample (4×10^{19} n/cm^2). These higher temperature irradiated samples also show lower unit cell volumes than the lower temperature irradiated samples for the similar fluences suggesting lower defect structure in the higher temperature irradiated samples. Isosurface volumes corresponding to the electron densities of the samples determined using F_O-Fourier synthesis however show a different variation. That is, isosurface volumes of 5×10^{18} and 4×10^{19} n/cm^2 samples irradiated at 52 °C are lower than the control sample and decrease with the increase in fluence. Sample irradiated to 2×10^{20} n/cm^2 show the highest isosurface volume. The isosurface volumes of the samples irradiated at 95 °C show a slight increase with the irradiation fluence and are greater than that of the control sample. The change in unit cell volumes are more relevant to the radiation-induced lattice expansions, while electron density maps and isosurface volumes can be used to understand the effects of radiation on local sites of the lattice. This is further discussed below.

Table 2. Fourier analyzed electron density measurements of calcite using a Level of 6 in ChimeraX and their Rietveld analyzed unit cell volumes. 'a.u.' refers to arbitrary units.

Sample	Fluence, T. (n/cm^2, °C)	Isosurface V (a.u.)	Unit cell volume from Rietveld analysis	
			V (Å^3)	σ_V (Å^3)
Control	N/A	12.44	366.742	0.004
C4	5×10^{18}, 52	12.03	369.371	0.005
C18	5×10^{18}, 95	12.63	369.194	0.018
Cb	4×10^{19}, 52	5.437	369.766	0.022
C10	4×10^{19}, 95	12.82	368.352	0.014
C6	2×10^{20}, 52	13.15	369.358	0.027

The isosurface volume variations of the electron densities determined in the samples are also depicted pictorially in Figure S3. Basically, the higher level of electron densities can be observed at Ca-sites than at C- and O-sites that are expected in the calcite lattice. A significant change in the electron density is observed in the 4×10^{19} n/cm^2, 52 °C sample in which C-/O-sites show the lowest level of electron densities. Even though this significantly low isosurface volume could be considered as an outlier, a similar change was also observed in dolomite samples. Since the lowest Bragg peak intensities (Figure 1),

lowest C-/O-site electron densities (Figure S3), and the highest unit cell volume (Table 2) are present in this sample, it is determined that the highest level of radiation-induced defect structure is present in this sample. These data further shows that local defect structure is comparable to that of the average. The difference in isosurface volumes are not significant to observe in Figure S3 for the rest of the samples. The presence of highest isosurface volume in 2×10^{20} n/cm^2 sample will be discussed later. However, comparatively larger unit cell volume and the highest isosurface volume in this 2×10^{20} n/cm^2 sample furthermore indicate that the effect of this highest neutron dose on calcite is significant.

Difference Fourier synthesis has shown that the topological details of electron densities are somewhat similar throughout the calcite lattice along different z sections due to its symmetry. Therefore, a z-section of 0.5 was selected to represent the summed electron densities of the samples in Figure 3. Approximate locations of Ca-, C-, and O-sites are highlighted in Figure 3a. The distribution and the level of electron densities in the control and those irradiated to 5×10^{18} n/cm^2 at 52 and 95 °C, and 4×10^{19} n/cm^2 52 °C samples are comparable with their corresponding unit cell volume changes (Table 2). These irradiated samples show bonding electrons in rings, especially at O-sites, which cannot be observed in the control sample. However, 4×10^{19} n/cm^2 95 °C sample shows more compact electron density distribution corresponding to Ca-sites. His sample also shows an increased electron density level, which is the highest among all the samples, at oxygen sites with the increased bonding electrons. Even though the 2×10^{20} n/cm^2 52 °C sample shows somewhat similar compact nature of electron density distribution, the bonding electron density at O-sites are comparable to that of the 5×10^{18} n/cm^2, 52 °C sample, indicating an analogous level of overall electron density to the change in unit cell volume of the two samples. Since this sample (2×10^{20} n/cm^2 52 °C) has the highest isosurface volume as well, it can be concluded that the level of local electron density sites are closely similar to its average values.

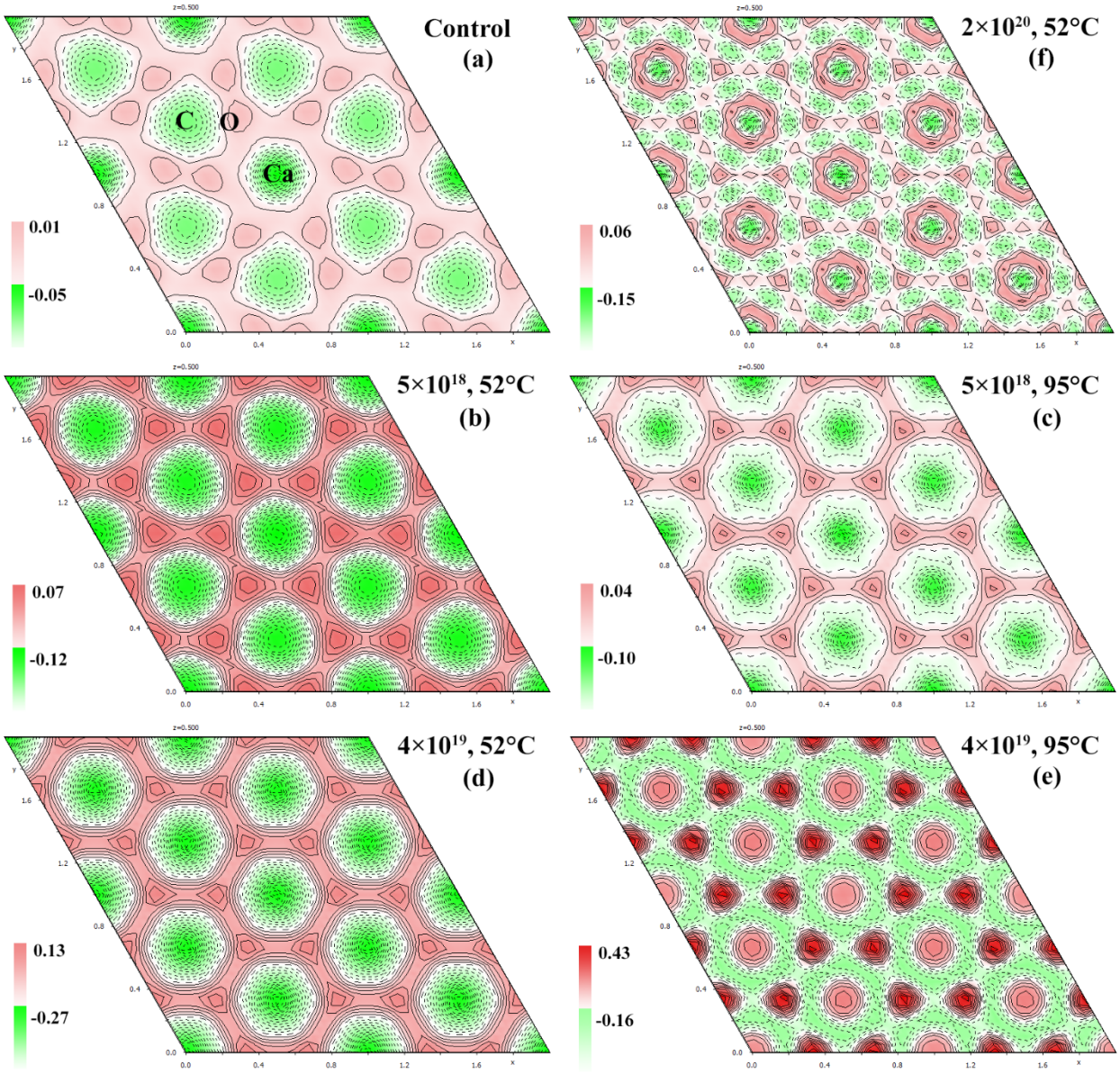

Figure 3. A pictorial presentation of the summation of difference Fourier synthesis of calcites. All sections are through the z = 0.5 plane. Positive and negative contours are shown using solid and dashed lines, respectively. Electron density levels are depicted using red for positive and green for negative color schemes. The red color scheme varies in a range of 0 – 0.43 and the green color scheme varies in a range of 0 – 0.27 arbitrary units, while 0.43 and 0.27 values are the highest electron density levels for positive and negative contours, respectively. Note that the electron densities at Ca- and C-sites can overlap due to orientation.

Microstrain (Ɛ) and the related dislocation density (ρƐ) of calcites calculated using microstrain and *d*-spacing of (104) Bragg reflection shows an increase with the increase in radiation considering 5×10^{18} and 2×10^{20} n/cm^2 doses at 52 °C (Table 3). The sample irradiated to 4×10^{19} n/cm^2 at 52 °C shows lower microstrain and the corresponding dislocation density than that of the control sample. Microstrain and the

corresponding dislocation density in samples irradiated to 5×10^{18} and 4×10^{19} n/cm^2 at the higher temperature (95 °C) are lower than the control sample and also of the samples with similar fluences irradiated at lower temperature (52 °C). The crystallite or the domain size (D) or the corresponding dislocation density (ρD) of calcites pre- and post-irradiated at 52 °C did not show any particular variation. A slight decrease in domain size and a corresponding increase in the ρD are present with the increase in fluence of the calcites irradiated at 95 °C. Similar microstrain-related characteristics are present in the data determined using (116) Bragg reflection. Domain size and ρD corresponding to (116) Bragg reflection also do not exhibit any particular variation. In both data sets, the largest domain size and the lowest dislocation density (ρD) are present in the 4×10^{19} n/cm^2, 52 °C sample. It is also notable that $\rho\varepsilon>\rho$D for all the samples. This indicates that the dislocations in calcites are in a piled up configuration rather than in a random spatial distribution.

Table 3. Crystallographic properties and radiation-induced dislocation densities of calcites corresponding to two Bragg reflections. Absolute value of a negative microstrain was used in C4 sample. R^2 are of the linear fits of the W-H plots.

Sample	Control	C4	Cb	C6	C18	C10
Irradiation, T. (n/cm^2, °C)	N/A	10^{18}, 52	10^{19}, 52	10^{20}, 52	10^{18}, 95	10^{19}, 95
R^2 of the linear fit	0.9056	0.7068	0.9624	0.9804	0.9808	0.7033
ε (%)	0.0668	0.0685*	0.0633	0.0856	0.0585	0.0497
	(104)					
$\rho\varepsilon$ (nm^{-2})	4.85E-01	5.07E-01	4.32E-01	7.92E-01	3.70E-01	2.67E-01
D (nm)	96.9	61.7	201.4	152.9	77.1	76.6
ρD (nm^{-2})	3.19E-04	7.88E-04	7.40E-05	1.28E-04	5.05E-04	5.11E-04
	(116)					
$\rho\varepsilon$ (nm^{-2})	1.27E+00	1.33E+00	1.13E+00	2.08E+00	9.70E-01	7.01E-01
D (nm)	80.7	107.6	116.6	91.1	77.1	78.7
ρD (nm^{-2})	4.61E-04	2.59E-04	2.21E-04	3.61E-04	5.05E-04	4.84E-04

4.1.2 Dolomite

As shown in Figure 4, no significant effect on the Bragg peaks of $CaMg(CO_3)_2$ phase is observed in the dolomite samples irradiated to 4×10^{19} at 52 °C and 5×10^{18} n/cm^2 at 95 °C, except for slightly decreased peak intensities compared to that of the unirradiated sample. However, the samples irradiated to 4×10^{19} n/cm^2 at 95 °C consist of significantly low-intensity peaks for some reflections such as (10-5) and

(20-1), while these peaks are missing in the sample irradiated to 2×10^{20} n/cm^2 at 52 °C. A decrease in the overall peak intensities with the increase in irradiation fluence can be observed in samples from both irradiation temperatures, while the lowest peak intensities are observed in the highest neutron dose (2×10^{20} n/cm^2) sample. Also a recovery of peak intensities is not observed in the similar neutron dose (4×10^{19} n/cm^2) samples irradiated at higher temperature from the lower temperature. This indicates that there is no annealing or healing effect as a result of high temperature irradiation on dolomite crystal structure contrast to that of the calcite.

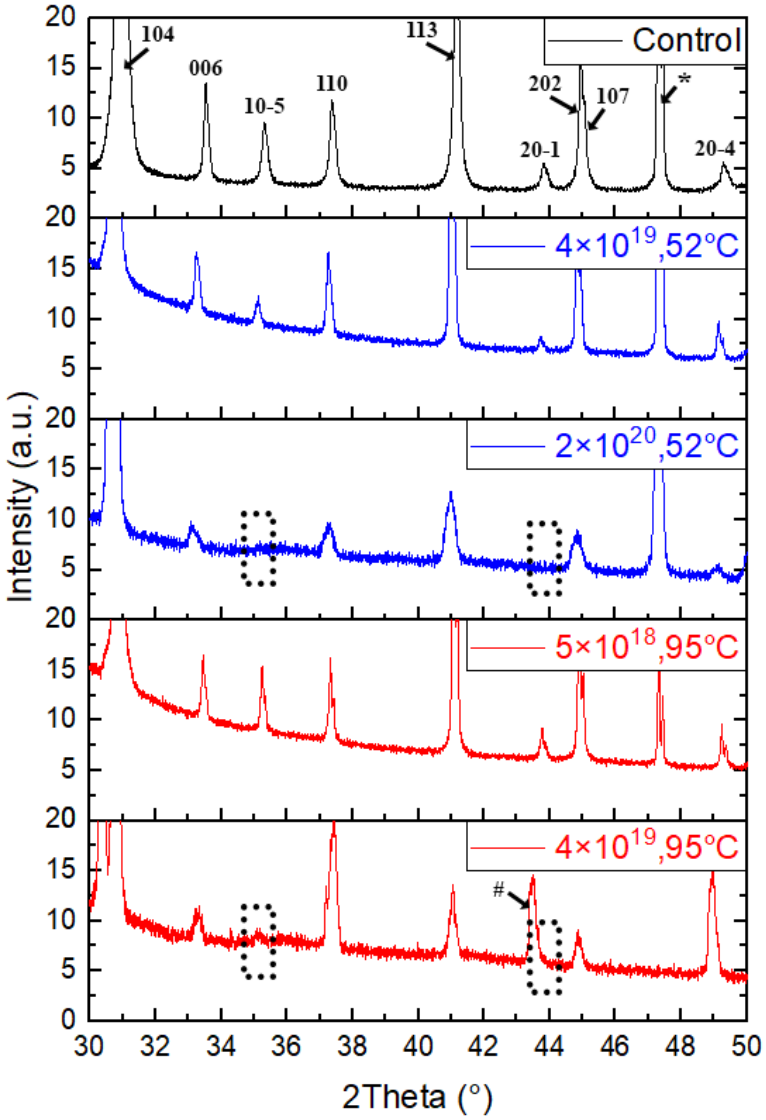

Figure 4. XRD patterns of dolomite samples. Only the 30 – 50° 2θ range is shown for clarity. A few peaks from standards are highlighted: * for Si and # for LaB_6. Note that (110), (20-1), and (20-4) peaks from dolomite overlap with (111), (200), and (210) of LaB_6, respectively. Rectangular boxes highlight the change in intensities of (10-5) and (20-1) peaks.

Both low temperature and high temperature irradiated dolomite samples showed an increase in lattice parameters (*a* and *c*) with the increase in irradiation (Figure 5). The highest increases in lattice parameters *a* and *c* are ~0.2 and ~1% for the irradiated samples compared to the unirradiated sample, respectively (Figure S2b). At closely similar neutron doses of 4×10^{19} n/cm^2, the largest lattice parameters *a* and *c* are in the sample irradiated at 95 °C, while the smallest lattice parameters among the irradiated samples are in the 5×10^{18} n/cm^2 irradiated at 95 °C sample.

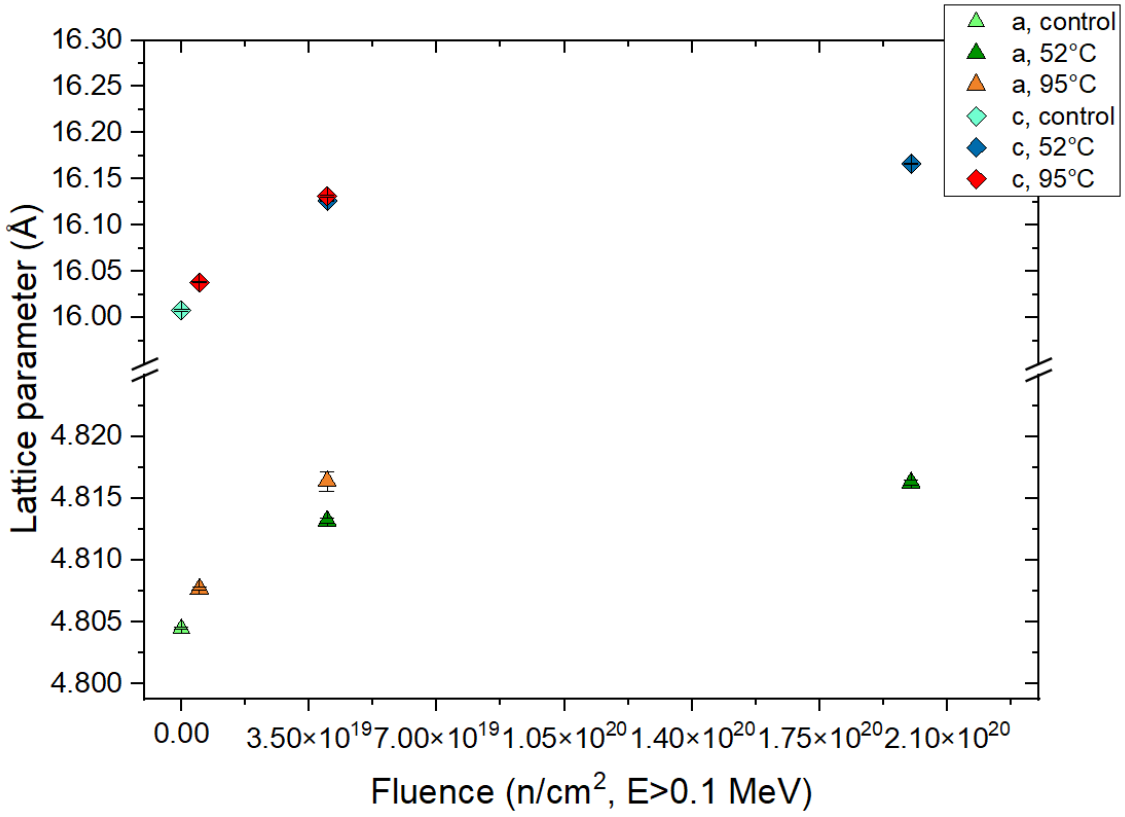

Figure 5. Refined lattice parameters of dolomite samples as a function of irradiation at 52 and 95 °C. Unirradiated sample is also shown.

The unit cell volumes (Table 4) of dolomites irradiated at both 52 and 95 °C increase with increasing neutron dose as expected due to the increase in lattice parameters. Isosurface volumes of the samples corresponding to the F_O-Fourier synthesis electron densities depicted in Figure S4 on the other hand show considerable variation as a function of irradiation. That is, the isosurface volumes of samples irradiated to 4×10^{19} n/cm^2 are lower than the control sample, while it is lowest in the sample irradiated at the higher temperature (95°C). The highest isosurface electron density volume is observed in the 5×10^{18} n/cm^2, 95 °C sample. Only a slight difference can be observed between the control sample and the sample irradiated

to 2×10^{20} n/cm^2 at 52 °C. The samples having lower isosurface volumes contain lower electron densities mostly at Mg sites as is highlighted in Figure S4. The decrease in electron densities is also observable at C-O sites, but the change in electron density is not significant at Ca sites. The low peak intensities in the XRD patterns, the low isosurface volumes or low electron densities at local sites, and the high unit cell volumes indicate the presence of high defect structure in these 4×10^{19} n/cm^2 samples. The considerably high isosurface volume and the largest unit cell volume in the 2×10^{20} n/cm^2 sample also indicate the presence of a high level of defect structure in it. These behaviors of dolomite samples are somewhat similar to that observed in the calcite samples, but the local structure defects of dolomites are more comparable to the isosurface volumes or local site electron densities whereas peak intensities in the XRD patterns and unit cell volumes are comparable with average defect structure.

Table 4. Fourier analyzed electron density measurements of dolomite using a Level of 6 in ChimeraX and their Rietveld analyzed unit cell volumes

Sample	Fluence, T.	Isosurface	Unit cell volume from Rietveld analysis	
	(n/cm^2, °C)	V (a.u.)	V (Å^3)	σ_V (Å^3)
Control	N/A	11.85	320.000	0.007
D18	5×10^{18}, 95	13.70	321.051	0.004
D15	4×10^{19}, 52	7.432	323.550	0.005
D13	4×10^{19}, 95	5.96	324.070	0.022
Dd	2×10^{20}, 52	11.98	324.764	0.016

The difference Fourier synthesis of the dolomite control sample in Figure 6a shows the comparatively high electron densities at Mg-sites. The relatively lower electron density sites of C are covered by these high negative contours of Mg-sites residing parallel to the C-sites in this orientation, while the bonding O-sites are observable. Slightly higher level of electron densities at Mg sites can be observed in the 5×10^{18} n/cm^2, 95 °C sample, but with lower electron densities at the bonding oxygen sites, indicating a change in the Mg-O (or C-O) bonding orientation along z-axis. Sample irradiated to 4×10^{19} n/cm^2 at 52 °C shows higher electron densities than the control sample and the 5×10^{18} n/cm^2, 95 °C sample. Some bonding characteristics in rings (Figure 6c) also start to show in this sample. In 4×10^{19} n/cm^2, 95 °C sample, more atomic sites with well-resolved electron densities are present than that of 4×10^{19} n/cm^2, 52 °C and all other samples. Even though the bonding characteristic in rings is also observed in this (4×10^{19} n/cm^2, 95 °C) sample, it is restricted to a smaller distance from the atomic sites compared to 4×10^{19} n/cm^2, 52 °C sample. Therefore, the nature of Mg-O bonding and electron density level in these two samples do not

have similar differences to that of the calcite samples irradiated to similar fluences. Electron densities are highest in the 2×10^{20} n/cm^2, 52 °C sample, but with scattered bonding character, especially at atomic O-sites.

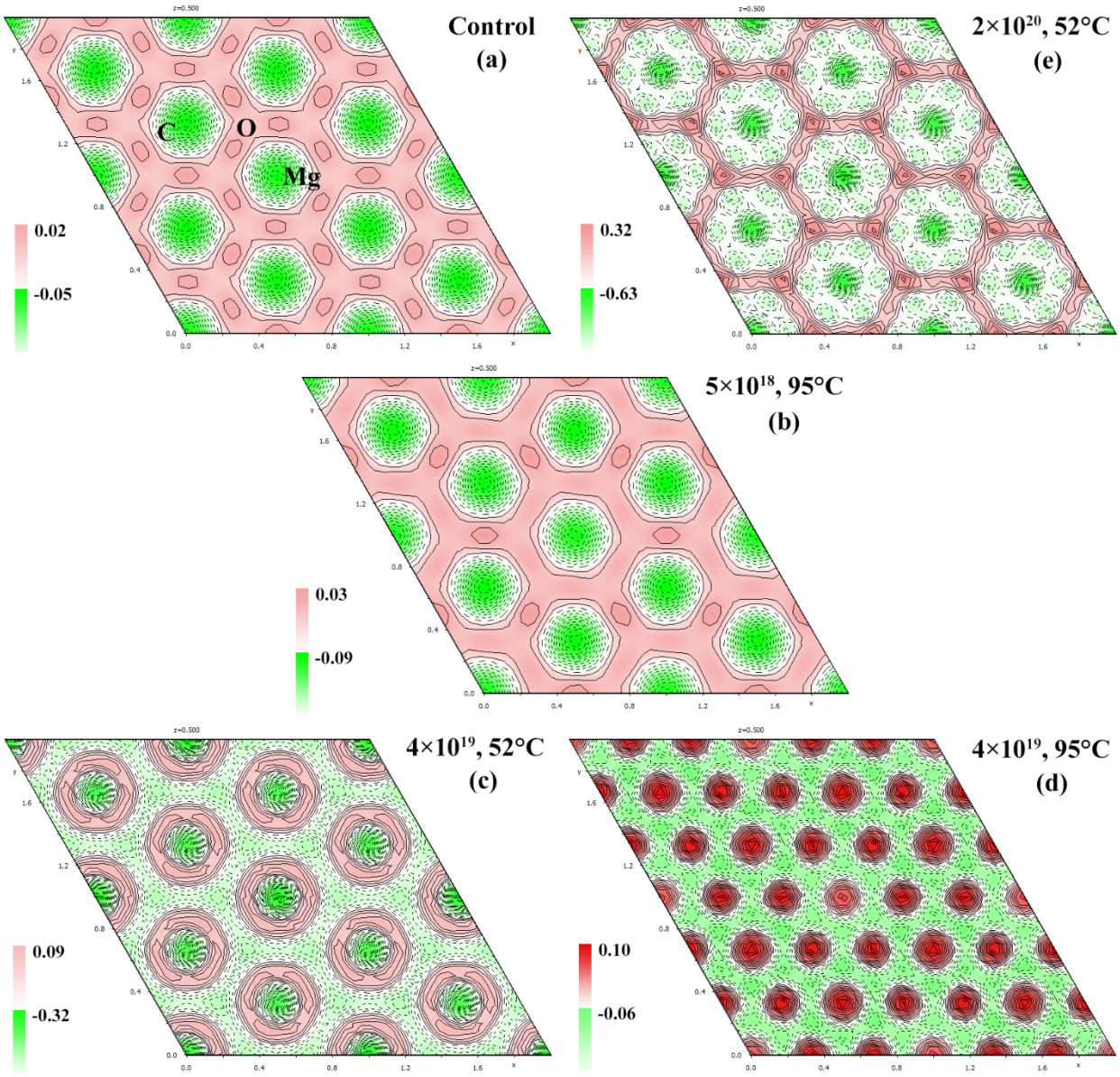

Figure 6. The summation of difference Fourier synthesis of dolomites through z = 0.5 plane.

In the irradiated dolomite samples, smaller domain size and the corresponding larger ρD than the control sample are present. An overall decrease in domain size and increase in ρD can be observed in the dolomite samples with the increase in irradiation. For 4×10^{19} n/cm^2 fluence, the higher temperature

irradiated sample shows the larger domain size and lower ρD than the lower irradiation temperature sample.

Table 5. Crystallographic properties and radiation-induced dislocation densities of dolomites corresponding to two Bragg reflections.

Sample	Irradiation, T.	(104)		(113)	
	(n/cm^2, °C)	D (nm)	ρD (nm^{-2})	D (nm)	ρD (nm^{-2})
Control	N/A	127.7	1.84E-04	86.9	3.98E-04
D15	4×10^{19}, 52	58.5	8.78E-04	64.9	7.11E-04
Dd	2×10^{20}, 52	39.8	1.89E-03	51.5	1.13E-03
D18	5×10^{18}, 95	61.6	7.92E-04	79.0	4.80E-04
D13	4×10^{19}, 95	91.9	3.55E-04	136.3	1.61E-04

4.2 Transmission electron microscopy

4.2.1 Calcite

TEM imaging of calcite samples both at pre- and post-irradiated conditions showed their crystalline characteristics. However, these samples also showed TEM beam damage. Two examples from the unirradiated control sample are shown in Figure S5. As shown in the SAED patterns of Figure S5a, the particle undergoes beam damage over time. The particle in Figure S5b showed mostly a single crystal area at the beginning of the TEM imaging. After its exposure to the beam, the particle showed some degradation (Figure S5c). A comparison of the SAED patterns of the particle at the two stages also showed a single crystal to polycrystalline transformation (patterns of rings with spots). The formation of ring patterns under the electron beam of calcites is usually reported as due to the formation of CaO.[26] However, the lattice fringe information of the nano-scale inclusions depicted in the HRTEM image (Figure S5d) mostly showed the existence of calcite microstructure. This suggests that if any CaO formed, it would reside in amorphous particle areas.

A particle from the ground calcite sample irradiated to 4×10^{19} n/cm^2 at 52 °C is shown in Figure 7a using BFTEM. This sample area mainly consists of a spotted SAED pattern corresponding to calcite in the [001] zone axis. The SAED pattern also consists of weak spotted Debye rings, which are more prominently observed (Figure 7f) at high-resolution. The corresponding HR image (Figure 7d) further shows that the particle consists of nano-scale crystalline inclusions. These inclusions show bright contrast in the corresponding DF image shown in Figure 7e compared to the rest of the particle area. These bright contrast inclusions also match the bright contrast areas observed in Figure 7b. Moreover, the lattice

fringes show that the inclusions correspond to different lattice orientations of calcite, indicating polycrystalline characteristics. Since electron beam can also damage calcites as was discussed above, the observation of these polycrystalline inclusions can be due to both neutron irradiation and electron beam damages.

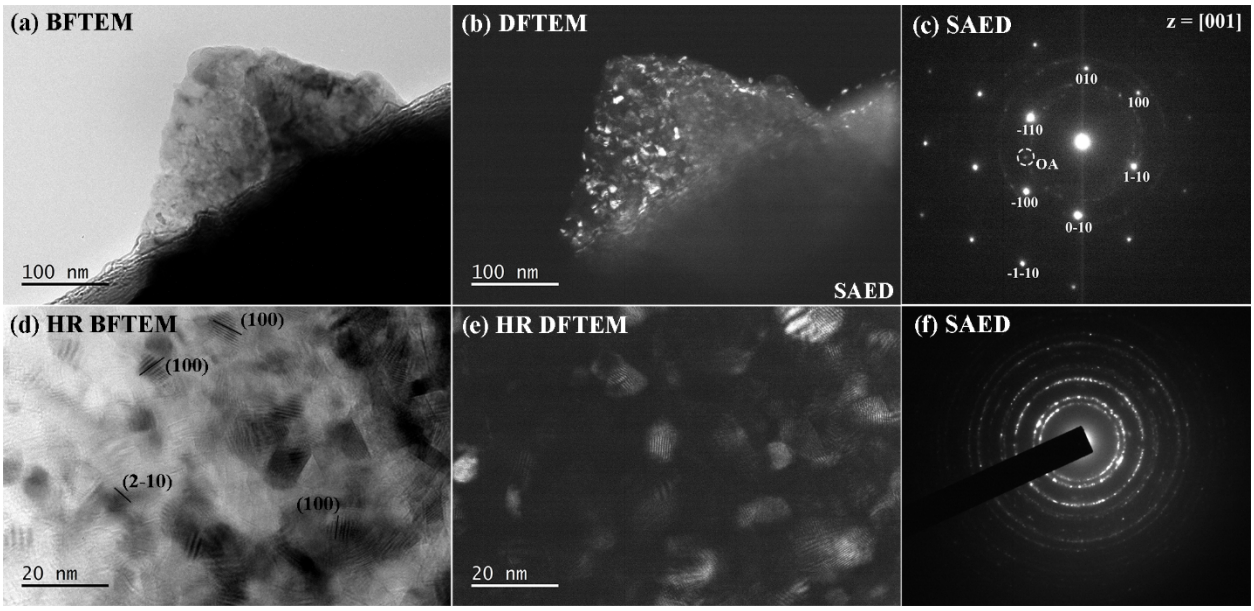

Figure 7. TEM images of a calcite sample neutron irradiated to 4×10^{19} n/cm^2 at 52 °C: (a-c) the full particle and (d-f) a selected area of the particle at HR. 'OA' in (c) indicates the objective aperture position in obtaining DF images.

4.2.2 Dolomite

A single crystal particle of an irradiated (4×10^{19} n/cm^2, 52°C) dolomite sample is shown in the BF and DF modes in Figure S6a-b. Several thinner particles of the sample also exhibit polycrystalline characteristics that lead to dense nano-scale inclusions (Figure S6c-d) like those observed in the images of calcite sample (Figure 7b, d, and e). Unirradiated samples also showed similar characteristics.

5.0 Discussion

Both calcite and dolomite have the same rhombohedral unit cell. However, calcite has a higher symmetry with a $R\bar{3}c$ space group compared to the $R\bar{3}$ space group in dolomite and hence more Bragg peaks are observed in the XRD pattern of dolomite. The CO_3^{2-} groups are layered in between Ca^{2+} cations in the calcite unit cell (Figure S7a), and every other layer of Ca^{2+} is replaced by Mg^{2+} in a dolomite unit cell (Figure S7b). In both these structures, the cation (Ca^{2+} or Mg^{2+}) bonds to six of O^{2-} anions of the CO_3^{2-} groups as depicted in Figure S7c. Since the electronegativity of magnesium (1.31 Pauling scale) is

greater than calcium (1.00 Pauling scale), it is expected that the bond lengths would be greater in Ca–O bonds (2.4848 Å in the unirradiated sample) than the Mg–O bonds (1.9991 Å in the unirradiated sample). Additionally, the effective ionic radii of Ca^{2+} and Mg^{2+} for a coordination number of VI are 1.00 and 0.720 Å, respectively. [27] As a result of these differences in Ca^{2+} and Mg^{2+} sites, a smaller unit cell is present in dolomite compared with that of calcite. Moreover, the dolomite unit cell contraction compared to the calcite is ~6 times greater along the c-axis than along the a- or b-axis. This difference in the decrease of the lattice parameter of dolomite can be attributed to the fact that every other layer of Ca^{2+} ions along c-axis are replaced by Mg^{2+} while keeping the Ca^{2+} unchanged in the unit cell border along a- and b-axes. It is also important to mention that these differences in the crystal structures may result in variances in the irradiation behavior of calcite and dolomite that are discussed below.

The decrease in Bragg peak (e.g., 006 peak) intensities in the XRD patterns of the irradiated calcite samples compared to the control sample indicates a radiation-induced decrease in the crystallinity, which usually occurs due to the decrease in the long-range order of the crystal structure. The missing Bragg peaks may also suggest some degree of structural disordering, which could be a result of radiation-induced atomic displacement, as no preferred orientation effect was observed in the XRD patterns of the samples. The abnormally lower isosurface volume corresponding to low C-/O- electron density sites together with the lowest peak intensities in the XRD pattern and largest unit cell volume obtained for the sample irradiated to 4×10^{19} n/cm^2 at 52 °C indicate that it has the highest defect structure among all calcite samples. The sample irradiated to 2×10^{20} n/cm^2 also showed a high defect structure characteristics from its high unit cell volume and low XRD peak intensities, but the electron densities of atomic sites both locally and at average did not show much variation like in the case of 4×10^{19} n/cm^2 at 52 °C sample. Higher irradiation temperature samples exhibited some healing effect on the crystallinity of calcites, which was indicated by slightly greater relative peak intensities in the samples irradiated at 95 °C than at 52 °C. Calcite samples irradiated from 5×10^{18} to 2×10^{20} at 52 °C and to 5×10^{18} at 95 °C consisted of anisotropic broadening at some peak tails. This could be another indication of radiation-induced decrease of crystallinity and/or an increase in the polycrystalline nature, which was observed using TEM analysis of the calcite samples in the post-irradiated condition.

In the case of dolomites, low peak intensities and the absence of some Bragg peaks in the XRD patterns of the samples irradiated to 2×10^{20} n/cm^2 at 52 °C and 4×10^{19} n/cm^2 at 95 °C were observed. Since some discrepancy in the peak intensities was present in the sample irradiated to 4×10^{19} n/cm^2 at 95 °C, a preferred orientation effect could contribute to the presence of its weak peak intensities or missing peaks in the XRD patterns. However, radiation-induced disordering of the dolomite crystal structure could be the major contributing factor in the absence of some peaks in the XRD patterns of the sample irradiated to 2×10^{20} n/cm^2 at 52 °C, since it did not show evidence of a preferred orientation effect. In

contrast to calcite, there is no indication of recovery of crystallinity in the dolomite samples due to an increase in the irradiation temperature. Like calcite, dolomite samples irradiated to 4×10^{19} n/cm^2, but at both 52 and 95 °C irradiation temperatures, also showed lower isosurface volumes mostly corresponding to the radiation damage at the Mg sites as was observed in the electron density maps. These two samples also showed a considerable amount of decrease in Bragg peak intensities and high unit cell volumes showing the presence of considerably high defect structures, especially in the sample irradiated at 95 °C. The largest unit cell volume and the lowest Bragg peak intensities on the other hand were observed in the highest dose (2×10^{20} n/cm^2) sample without a considerable level of decrease in the isosurface volume. These observations suggest that the average defect structure in dolomite corresponds to the Bragg peak intensities and unit cell volumes, while defects at local sites correspond to the isosurface volumes or local electron densities.

As a result of the energy deposition on crystals during irradiation creating defect structure, lattice growth is usually expected in most post-irradiated samples. For calcites, all the post-irradiated samples exhibited larger lattices compared to the unirradiated samples. However, uninterrupted increases in the calcite lattice parameters as a function of irradiation at both 52 and 95 °C were not observed. After the lattice growth of ~0.2 % increase compared to the unirradiated sample observed for the sample irradiated to 5×10^{18} n/cm^2 (E>0.1 MeV), only slight changes in both *a* and *c* lattice parameters were observed for the samples irradiated to 4×10^{19}–2×10^{20} n/cm^2 at 52 °C (Table S1). Although the increase in the lattice parameters is comparatively smaller, the samples irradiated at 95 °C also showed similar behavior to that of the samples irradiated at 52 °C with similar neutron doses. The change in lattice parameters of the irradiated samples compared to the unirradiated sample showed a 0.02 % decrease for samples irradiated at 52 °C and a 0.07 % decrease for samples irradiated at 95 °C with the increase in irradiation fluences from 5×10^{18} to 2×10^{20} n/cm^2 and from 5×10^{18} to 4×10^{19} n/cm^2, respectively. A greater effect was observed on the irradiated calcite lattices along c-axis as the increase in *c* lattice parameter compared to the unirradiated sample was 0.3–0.5 % at 52 °C and 0.2–0.3 % at 95 °C. This could be due to the comparatively greater amount of atomic layers along the c-axis (Ca–Ca bond length is 4.0440 Å for the unirradiated sample) than along a- or b-axis (Ca–Ca bond length is 4.9834 Å) as a result of the symmetry of calcite, allowing more energy to be deposited along c-axis than along a- or b-axis. The O-Ca-O or Ca-O-Ca bond angles (Table S2) do not show changes that would reflect this greater increase of lattice parameter along c-axis, indicating a possible cancelling out of lattice expansion effects in the two directions (a or b- and c-axes) due to the interconnectivity of atoms of these two types of bonding. However, an increase in the stand-alone Ca-O-C bond angles resulting in a tilt of the O-C-O bonds reflected the greater lattice expansion along c-axis. The O-C-O bonding angles did not show any changes in the calcite samples. Furthermore, the difference Fourier synthesis showed lower electron densities at

Ca-sites and greater interaction or short length between Ca-O bonding, which is indicated by more bonding electrons at O-sites, as another reason for a lower unit cell volume of 4×10^{19} n/cm^2 95 °C sample compared to the rest of the irradiated samples. Moreover, the bonding electrons in rings and more compact (high) electron densities at atomic O-sites in the irradiated samples may be a result of the O-C-O bond tilt observed in these samples. Such rings of bonding electrons at O-sites were recenetly described as due to the vibration of two different oxygen sites at their mean positions on the plane of carbon using a joint probability density function study of high temperature structures of calcite. [28] According to this study, the bonding electron rings of CO_3 groups facilitate the minimization of the repulsion between the Ca-O bonding electrons. This implies that the assymetric unit cell expansion occurred as a result of radiation (the current study) acts somewhat similar to the impacts of high temperature on calcites.

The observation of lower lattice growth at the irradiation temperature of 95 °C may also indicate that the irradiation temperature has some healing effect on the calcite by relieving some of the stress resulted by the energy deposited on the lattices during irradiation. The lattice healing behavior of calcite at higher irradiation temperature is similar to what was observed in quartz, which displaced comparatively greater reduction in the radiation-induced expansion at higher irradiation temperatures.[18, 29] Lower microstrain and the corresponding dislocation density ($\rho\mathcal{E}$) were also observed in the calcite samples irradiated at similar fluences but at higher temperature (95 °C) than the lower temperature (52 °C). This reduction in lattice strain further suggests a healing effect of the calcites irradiated at 95 °C. Even though the crystallite size or the related dislocation density (ρD) of calcites did not show a relationship with irradiation, the sample irradiated to 4×10^{19} n/cm^2 at 52 °C showed the largest crystallite size and the corresponding lowest dislocation density (ρD). Since this sample also has the largest lattice parameter along c-axis and the lowest electron density at C-sites, it can be inferred that the crystal growth along c-axis was induced to accommodate the radiation-induced defect structure. A similar lattice growth is observed in the 2×10^{20} n/cm^2, 52 °C sample showing the effect of increased neutron dose on calcite. These samples also did not show significant improvement in the crystallinity indicating the calcite domain growth resulted purely from radiation-induced defect structure, which is mainly constructed by piled up dislocation configuration showed by $\rho\mathcal{E}>\rho$D.

Unlike the calcite samples, dolomite samples exhibited a continuous lattice growth with the increase in irradiation up to 2×10^{20} n/cm^2 (E>01. MeV). The lattice parameter increase is greater along c-axis than along a-axis for dolomites, as was observed in calcites. Compared to calcites, this increase is greater in dolomites, indicating that the radiation-induced energy deposition in the structure along c-axis is greater in dolomites (Ca–Mg bond length along c-axis of the unirradiated dolomite is 3.8487 Å). The comparatively lower electron density at Mg-sites observed in the F_O-Fourier synthesis also verifies this statement, while suggesting Mg-sites are more radiation sensitive than Ca-sites. As observed in calcites,

dolomite samples also showed the tilting of CO_3 group observed by the change in Ca-O-C or Mg-O-C bond angles in the irradiated samples (Table S3). It is also observed that Ca-O-C and Mg-O-C bond angles change in the opposite directions with respect to the lattice expansion due to irradiation. This assymetric undulation at Ca- and Mg- sites resulted in a tilt and a deformation of the CO_3^{2-} bonding unlike in the calcite samples, indicating that the dolomite samples to have a greater repulsion between Ca and Mg with O electrons. This is apparent in the 4×10^{19} n/cm^2, 52 °C and 5×10^{18} n/cm^2, 95 °C samples, where the difference between Ca-O-C and Mg-O-C bond angles is >30° with the greatest change in O-C-O bnd angles compared to the control sample (Table S3). The greater low electron densities at O-sites (e.g., in 5×10^{18} n/cm^2, 95 °C sample) and more compact electron density sites in dolomite samples than in calcite samples also indicate the extra CO_3^{2-} bond deformation in the dolomites rather than just having a tilting as in the calcites. However, the F_0-Fourier electron density maps did not show any decarbonation due to tilting and/or deformation of CO_3 groups in either calcites or dolomites. Additionally, larger lattice parameters both along a/b- and c-axes were obtained for the similar neutron dose dolomite samples irradiated at 95 than at 52 °C, showing less irradiation temperature dependence in dolomite. Furthermore, the crystallite size decrease and the corresponding dislocation density increase with the increase in irradiation fluence are consistent with the other crystallographic characteristics present in dolomite samples. The larger domain size and the smaller ρD observed in 4×10^{19} n/cm^2 sample irradiated at 95 °C than that of the 52 °C sample showed some healing effect of the defect sturcture, but it was not significant enough to lower the radiation-induced effects on the lattice growth or the samples' crystallinity. Therefore, it can be concluded that the irradiation temperature does not have a significant healing effect on dolomite in contrast to calcite.

These results are in agreement with mechanical property measurements of irradiated calcite and dolomite samples with a similar range of fluences.[3, 15, 16, 30] For example, nanohardness values for dolomite decreased with increasing fluence—however, those values decreased more sharply at lower fluence before the decrease slowed at doses >1×10^{19} n/cm^2.[3] Moreover, the change in calcite hardness with fluence was small, but the calcite samples showed less scatter.[3] Pignatelli et al. [12] demonstrated that disordered concrete aggregates are prone to greater chemical reactivity because quartz undergoes radiation-induced amorphization [18] and therefore, a higher chemical reactivity. They also postulated that the lower chemical reactivity in calcite (and dolomite) could be attributed to its ability to retain crystallographic order under irradiation, as was later shown elsewhere.[31] Another study carried out on irradiation of calcite-water media also reported a dissolution of calcite.[32] Although significant amorphization was not observed in the irradiated calcite and dolomite samples in this current study, the notable crystallographic disorder in the two analogues might be enough for their radiation-induced chemical reactivity.

Even though the unirradiated calcite samples showed some beam damage under TEM, the calcite structure was retained as nano-scale inclusions exhibiting polycrystalline characteristics, and no evidence was observed for the formation of CaO as a crystalline phase due to the decomposition of calcite under electron beam, as is described in the literature. [26, 33, 34] TEM analysis of irradiated calcites also showed crystalline characteristics as exhibited in the high density polycrystalline character observed with high-resolution TEM imaging. Therefore, it can be concluded that no significant decomposition of calcite into its crystalline pseudomorphs such as CaO was observed using microstructural investigations and XRD studies. Similar microstructural characteristics were observed in dolomites to that found in the calcites. That is, no radiation-induced degradation leading to decomposition of dolomite structure was observed.

Ion irradiation studies have shown that calcite could undergo carbonate ion bond breakage and phase transformation. Based on Raman and Fourier transform infrared (FTIR) characterization of ion irradiated (1×10^{11} to 1×10^{13} ions/cm^2 fluence, 100 MeV Ag^{8+}) calcite, it could undergo carbonate ion bond breakage.[35] Another study by the same group reported ion irradiation (5×10^{12} ion/cm^2 fluence, 120 MeV Au^{9+}) induced phase transformation of calcite into vaterite, a polymorph of $CaCO_3$.[36] However, neutron irradiation of calcite up to 2×10^{20} n/cm^2 at E>0.1 MeV showed no apparent bond breakage or phase transformation based on XRD and TEM data in this current study. Another study on gamma irradiation of hardened cement paste (HCP) showed radiation-induced carbonation of HCP resulting in an increase in the amount of calcite and a decrease in the amount of portlandite ($Ca(OH)_2$) with the increase in gamma radiation from 0.1 to 1 MGy (^{60}Co).[37] This also showed that calcite is less sensitive to radiation damage under high energy (E > 0.1 MeV) compared to other mineral aggregates in cement.

6.0 Conclusions

XRD studies demonstrated radiation-induced disordering or a decrease in the long-range periodicity of the crystal structure that resulted in a decrease in Bragg peak intensities and crystallinity of both calcite and dolomite samples irradiated up to 2×10^{20} n/cm^2 at 52 °C and 4×10^{19} n/cm^2 at 95 °C (E>0.1 MeV). A slightly higher Bragg peak intensities was observed in the XRD patterns of calcite samples irradiated at 95 °C than that of at 52 °C, indicating an irradiation temperature healing effect. This was not observed in the dolomite samples. Furthermore, both concrete aggregate analogues exhibited lattice growth in their post-irradiation condition. The significance of increase in lattice parameters in the calcite samples decreased after a 5×10^{18} n/cm^2 dose. However, a continuous increase in the lattice parameters with increasing irradiation was observed in dolomite samples. While dislocation densities calculated using XRD data did not show a clear relationship to the irradiation conditions, lower dislocation densities calculated from microstrain were observed in the higher temperature irradiated calcite samples. On the other hand, an increase in dislocation density calculated using crystal domain size was observed in the

dolomite samples. Thus, a reduction in swelling and lattice strain were only observed in calcite samples as a result of partial annealing due to the higher irradiation temperature.

F_O-Fourier synthesis also showed that Mg-sites are more prone to irradiation damage than Ca, possibly due to the greater energy deposition along the c-axis than either along the a- or b-axes of the dolomite unit cell. This also resulted in a radiation-induced asymmetric lattice expansion. A tilting effect of CO_3 groups in calcite and both tilting and deformation effects of CO_3 group in dolomite also observed due to this asymmetric lattice expansion.

Lattice growth and some radiation-induced disorder in the post-irradiated calcite and dolomite show that physical and chemical properties of concrete aggregates composed of these materials can be deleteriously affected, but to a much smaller extent than quartz or silicates, during prolonged NPP operations. Furthermore, the irradiation effects are not enough to structurally decompose the samples into other pseudomorphs such as CaO at least into a crystalline form that can be observed in XRD and TEM or to transform calcite into its aragonite and vaterite polymorphs.

Supporting Information:

Figure S1. Full profile fits of (a) calcite and (b) dolomite control samples performed using Rietveld analysis. The asterisk in figure (a) depicts an impurity peak.

Figure S2. Percent change in lattice parameters of (a) calcite and (b) dolomite samples with respect to their control samples.

Figure S3. Electron density maps of calcites calculated using F_O-Fourier synthesis. Maps are shown along [006] direction at an isosurface level of 6 together with a model. . Different colors are used for different samples with no color scale corresponding to the density levels. The model is drawn to indicate the approximate elemental locations.

Figure S4. Electron density maps of dolomites calculated using F_O-Fourier synthesis. Maps are shown along [20-1] direction together with a model. Some of the Mg atoms are highlighted by arrows and a rectangle in 10^{19} n/cm^2 samples.

Figure S5. (a) BFTEM and SAED patterns of a particle of the unirradiated calcite sample. (b) Another calcite particle just after and (c) after 5 – 10 min exposure to the beam. (d) HR-BFTEM image of the post exposure particle in (c).

Figure S6. TEM images of two selected particles from irradiated (4×10^{19} n/cm^2, 52°C) dolomite sample.

Figure S7. The rhombohedral unit cells of (a) calcite and (b-c) dolomite. Note that two unit cells along c-axis are shown in (b).

Table S1. Refined lattice parameters of the calcite samples.

Table S2. Bond angles of calcite samples.

Table S3. Bond angles of dolomite samples.

SFC#. Separate files of the atomic coordinates, displacement parameters, and the structure factors of calcite samples obtained from Jana2006 software are attached separately.

SFD#. Separate files of the atomic coordinates, displacement parameters, and the structure factors of dolomite samples obtained from Jana2006 software are attached separately.

7.0 ACKNOWLEDGMENTS

This research was supported in part by the US DOE, Office of Nuclear Energy, Light Water Reactor Sustainability Program under contract DE-AC05-00OR22725 with UT-Battelle, LLC, via ORNL. This work was also performed under the auspices of the U.S. Department of Energy (DOE) by Lawrence Livermore National Laboratory (LLNL) under Contract No. DE-AC52-07NA27344. The authors also wish to thank Kevin Field, Alain Giorla, Patricia Tedder, Luis Mora, and Stephanie Curlin for their technical support.

8.0 References

[1] Graves, H.; Le Pape, Y.; Naus, D.; Rashid, J.; Saouma, V.; Sheikh, A.; Wall, J. Expanded Material Degradation Assessment (EMDA), Volume 4: Aging of Concrete, NUREG/CR-7153, ORNL/TM-2011/545. U.S. Nuclear Regulatory Commission, 2014.

[2] Rosseel, T. M.; Wall, J. J.; Field, K. G.; Pape, Y. Le; Naus, D. J.; Remec, I. ; Busby, J. T.; Bruck, P. Radiation damage in reactor cavity concrete. In Fontevraud 8 - Contribution of Materials Investigations and Operating Experience to LWRs' Safety, Performance and Reliability, September 14-18, 2014; Avignon, France, 2014.

[3] Rosseel, T. M.; Gussev, M. N.; Mora, L. F. The Effects of Neutron Irradiation on the Mechanical Properties of Mineral Analogues of Concrete Aggregates, Proceedings of the 18th International Conference on Environmental Degradation of Materials in Nuclear Power Systems – Water Reactors, Jackson, J.; Paraventi, D.; Wright, M. Eds. *The Minerals, Metals & Materials Series.* **2019,** *2,* 151-161 https://doi.org/10.1007/978-3-319-68454-3_14.

[4] Kontani, O.; Ichikawa, Y.; Ishizawa, A. Irradiation Effects on Concrete Durability of Nuclear Power Plants, May 2–5, 2011; Proceedings of ICAPP 2011, Nice, France, 2011.

[5] Fillmore, D. L. Literature Review of the Effects of Radiation and Temperature on the Aging of Concrete. United States: N. p., 2004. Web. doi:10.2172/910954.

[6] Pape, Y. Le; Field, K.G.; Remec, I. Perspective on Radiation Effects in Concrete for Nuclear Power Plants — Part II: Perspective from Micromechanical Modelling. *Nucl. Eng. Des.* **2015,** *282,* 144-157.

[7] Missouri department of Natural Resources, Division of Geology and Land Survey, The Geologic Column of Missouri, Vol. 1, Issue 1, 2006.

[8] Maruyama, I.; Kontani, O.; Takizawa, M.; Sawada, S.; Ishikawa, S.; Yasukouchi, J.; Sato, O.; Etoh, J.; Igari, T. Development of soundness assessment procedure for concrete members affected by neutron and gamma-ray irradiation. *J. Adv. Concr. Technol.* **2017,** *15,* 440-523.

[9] Park, K.; Kim, H-T.; Kwon, T-H.; Choi, E. Effect of neutron irradiation on response of reinforced concrete members for nuclear power plants. *Nucl. Eng. Des.* **2016,** *310,* 15-26.

[10] Kabacinska, Z.; Yate, L,; Wencka, M,; Krzyminiewski, R.; Tadyszak, K.; Coy, E. Nanoscale Effects of Radiation (UV, X‑ray, and γ) on Calcite Surfaces: Implications for its Mechanical and Physico-Chemical Properties. *J. Phys. Chem. C* **2017,** *121,* 13357−13369.

[11] Bruck, P.; Esselman, T.; Expected Condition of Concrete at Age 80 Years of Reactor Operation. Technical Report A13276-R-001, 2013, Lucius Pitkin, Inc.

[12] Pignatelli, I.; Kumar, A.; Field, K. G.; Wang, B.; Yu, Y.; Pape, Y. L.; Bauchy, M.; Sant, G. Direct experimental evidence for differing reactivity alterations of minerals following irradiation: the case of calcite and quartz. *Sci. Rep.* **2016,** *6:20155*, 1-10.

[13] Maruyama, I.; Kontani, O.; Sawada, S.; Sato, O.; Igarashi, G.; Takizawa, M. Evaluation of Irradiation Effects on Concrete Structure - Background and Preparation of Neutron Irradiation Test. Proceedings of the ASME 2013 Power Conference POWER2013, Boston MA, USA, 2013.

[14] Rosseel, T.M.; Maruyama, I.; Le Pape, Y.; Kontani O.; Giorla, A.; Remec, I.; Wall, J.J.; Sircar, M.; Andrade, C.; Ordonez, M. Review of the Current State of Knowledge on the Effects of Irradiation on Concrete, *J. Adv. Concr. Technol.* **2016,** *14,* 368-383.

[15] Seeberger, J.; Hilsdorf, H. Einfluß von radioactiver Strahlung auf die Festogkeit and Struktur von Beton. Institut für Massivbau and Baustofftechnologie, Universität Karlsruhe, 1982.

[16] Field, K. G.; Remec, I.; Le Pape, Y. Perspective on radiation effects in concrete for nuclear power plants—Part I: Quantification of radiation exposure and radiation effects. *Nucl. Eng. Des.* **2015,** *282,* 126-143.

[17] ASTM C 294-12, Standard Descriptive Nomenclature of Constituents of Natural Mineral Aggregates. Annual Book of Standards, ASTM International, West Conshohocken, PA, 2017.

[18] Silva, C.; Rosseel, T. M.; Kirkegaard, M. C. Radiation-Induced Changes in Quartz, A Mineral Analog of Nuclear Power Plant Concrete Aggregates. *Inorg. Chem.* **2018**, *57,* 3329–3338.

[19] Larson, A.C.; Von Dreele, R.B. General Structure Analysis System (GSAS). Los Alamos National Laboratory Report LAUR 86-748, 2000.
[20] Petricek, V.; Dusek, M.; Palatinus, L. Crystallographic computing system Jana2006: General features. *Z. Kristallogr.* **2014,** *229,* 345-352.
[21] Pettersen, E. F.; Goddard, T. D.; Huang, C. C.; Meng, E. C.; Couch, G. S.; Croll, T. I.; Morris, J. H.; Ferrin, T. E. UCSF ChimeraX: Structure visualization for researchers, educators, and developers. *Protein Sci.* **2021,** *30,* 70-82.
[22] Silva, C. M.; Ibrahim, F.; Lindquist, E. G.; McMurray, J. W.; Bryan, C. D. Brittle Nature and the Related Effects of Zirconium Hydrides in Zircaloy-4. *Mater. Sci. Eng. A*, **2019,** *767*, 138396.
[23] Holt, R. A. Recovery of cold-work in extruded Zr-2.5 wt% Nb. *J. Nucl. Mater.* **1976,** *59,* 234-242.
[24] Momma, K.; Izumi, F. VESTA 3 for Three-Dimensional Visualization of Crystal, Volumetric and Morphology Data. *J. Appl. Crystallogr.* **2011,** *44,* 1272-1276.
[25] Silva, C.; Ma, L.; Hammers, O.; Lindle, D. Microstructural characterization of precipitation-synthesized fluorapatite nano-material by TEM using different sample preparation techniques. *Micron*, **2008,** *39,* 269-274.
[26] Hooley, R.; Brown, A.; Brydson, R. Factors affecting electron beam damage in calcite nanoparticles. *Micron*, **2019,** *20,* 25-34.
[27] Shannon, R. D. Revised effective ionic radii and systematic studies of interatomic distances in halides and chalcogenides. *Acta Cryst.* **1976,** *A32,* 751-767.
[28] Ishizawa, N.; Setoguchi, H.; Yanagisawa, K. Structural evolution of calcite at high temperatures: Phase V unveiled. *Sci. Rep.* **2013,** *3,* 2832.
[29] Bykov, V. N.; Denisov, A. V.; Dubrovskii, V. B.; Korenevskii, V. V.; Krivokoneva, G. K.; Muzalevskii, L. P. Effect of Irradiation Temperature on the Radiation Expansion of Quartz. *Sov. Atom. Energy*, **1981,** *51,* 593-595.
[30] Hilsdorf, H.; Kropp, J.; Koch, H. The effects of nuclear radiation on the mechanical properties of concrete. *Spec. Publ. Am. Conc. Inst.* **1978,** *55,* 223-254.
[31] Hsiao, Y-H.; Wang, B.; La Plante, E. C.; Pignatelli, I.; Krishnan, N. M. A.; Pape, Y. Le; Neithalath, N.; Bauchy, M,; Sant, G. The effect of irradiation on the atomic structure and chemical durability of calcite and dolomite. *NPJ Mater. Degrad.* **2019,** *3,* 36.
[32] Costagliola, A.; Vandenborre, J.; Blain, G.; Baty, V.; Haddad, F.; Fattahi, M.; Radiolytic dissolution of calcite under gamma and helium ion irradiation. *J. Phys. Chem. C.* **2017,** *121,* 24548-24556.
[33] Rodriguez-Navarro, C.; Kudłacz, K.; Cizer, Ö.; Ruiz-Agudo, E. Formation of amorphous calcium carbonate and its transformation into mesostructured calcite. *Cryst. Eng. Comm.* **2015,** *17,* 58-72.
[34] Rodriguez-Navarro, C.; Ruiz-Agudo, E.; Luque, A.; Rodriguez-Navarro, A. B.; Ortega-Huertas, M. Thermal decomposition of calcite: Mechanisms of formation and textural evolution of CaO nanocrystals. *Am. Mineral.* **2009,** *94,* 578-593.
[35] Nagabhushana, H.; Prashantha, S. C.; Nagabhushana, B. M.; Lakshminarasappa, B. N.; Singh, F. Damage creation in swift heavy ion-irradiated calcite single crystals: Raman and Infrared study. *Spectrochim. Acta A*. **2008,** *71,* 1070.
[36] Nagabhushana, H.; Nagabhushana, B. M.; Lakshminarasappa, B. N.; Singh, F.; Chakradhar, R. P. S. Swift heavy ion irradiation induced phase transformation in calcite single crystals. *Solid State Commun.* **2009,** *149,* 1905-1908.
[37] Vodak, F.; Vydra, V.; Trtik, K.; Kapickova, O. Effect of gamma irradiation on properties of hardened cement paste. *Mater. Struct.* **2011,** *44,* 101-107.